JOURNAL OF PROPULSION AND POWER
Vol. 23, No. 2, March–April 2007

Investigation of Metallized and Nonmetallized Hydroxyl Terminated Polybutadiene/Hydrogen Peroxide Hybrid Rockets

E. Farbar*
Carleton University, Ottawa, Ontario K1S 5B6, Canada
J. Louwers†
Cesaroni Technology, Inc., Gormley, Ontario L0H 1G0, Canada
and
T. Kaya‡
Carleton University, Ottawa, Ontario K1S 5B6, Canada

DOI: 10.2514/1.22091

Results from 15 static test firings of lab scale hybrid rocket motors using 90% concentrated unstabilized hydrogen peroxide as an oxidizer with hydroxyl terminated polybutadiene fuel are presented. Thirteen of those tests used aluminum or aluminum/magnesium alloy additive in the fuel. The performance characteristics of the propellant combinations were determined. The experimental results indicated combustion efficiencies of 0.72–0.89 and regression rates of 0.5–1.3 mm/s for the metallized fuel combinations. A correlation of the regression rate data for the metallized propellants deviated from that which was derived for turbulent convective heat transfer dominated behavior. A numerical model of the hydrogen peroxide/nonmetallized hydroxyl terminated polybutadiene motor was built using a commercial computational fluid dynamics code. The model was combined with an in-house code to predict the regression rate of the propellant combination, and the flowfield characteristics at the initial operating conditions for two of the experimental tests. The results of the model indicated that the proposed numerical model is a promising tool for mapping the temporal and spatial variation of the regression rate in hybrid motors operating with homogeneous hydrocarbon fuels.

Nomenclature

A_{port}	=	fuel port area, m^2
A_{venturi}	=	venturi throat area, m^2
$a_{g,j}$	=	gray gas j weight or amplitude
C_d	=	venturi loss coefficient
Cf	=	thrust coefficient
Cp	=	isobaric specific heat, $J/kg \cdot K$
c^*	=	characteristic velocity, m/s
D	=	diffusion coefficient, m^2/s
D_{port}	=	fuel grain port diameter, m
D_{throat}	=	nozzle throat diameter, mm
$D_{\text{prechamber}}$	=	precombustion chamber port diameter, m
F	=	thrust, N
G	=	mass flux, $kg/m^2 \cdot s$
g	=	gravitational acceleration, m/s^2
h	=	enthalpy, m^2/s^2
I_{sp}	=	specific impulse, s
K_j	=	monochromatic absorption coefficient for gas j, $1/Pa \cdot m$
k	=	turbulence kinetic energy, m^2/s^2
L	=	length, m
L^*	=	characteristic reaction chamber length, m
M	=	mass, kg
M_{inert}	=	mass of precombustion and reaction chambers, kg
N_c	=	number of components in gas mixture
N_g	=	number of gray gases
O/F	=	mass oxidizer to fuel ratio
P, p	=	pressure, Pa
p_jL	=	product of the partial pressure and path length of gas j, $Pa \cdot m$
q	=	heat flux, $J/m^2 \cdot s$
R_u	=	universal gas constant, $J/mol \cdot K$
$\dot{r}$	=	fuel regression rate, mm/s
S	=	source term in species conservation equation, $kg/m^3 \cdot s$
T	=	temperature, K
t	=	time, s
u, v, w	=	velocity components, m/s
x, y, z	=	Cartesian axes, m
Y_i	=	mass fraction of fluid component i
Γ	=	diffusivity, $kg/m \cdot s$
γ	=	ratio of specific heats
ε	=	turbulence energy dissipation, m^2/s^3
ϵ_g	=	total emissivity of gas mixture
η	=	efficiency
λ	=	thermal conductivity, $W/m \cdot K$
μ	=	dynamic viscosity, $Pa \cdot s$
ν'	=	stoichiometric coefficient of reactant
ρ	=	density, kg/m^3
ω	=	turbulence eddy frequency, $1/s$

Subscripts

a	=	action
amb	=	ambient conditions
c	=	chamber
f	=	final, fuel

Received 28 December 2005; revision received 18 July 2006; accepted for publication 18 August 2006.

*Research Assistant, Mechanical and Aerospace Engineering Department, 1125 Colonel By Drive; currently Research Assistant, Aerospace Engineering Department, University of Michigan, Ann Arbor, MI 48109. AIAA Student Member.

†Program Manager, Propulsion Systems, 2561 Stouffville Road.

‡Professor, Mechanical and Aerospace Engineering Department, 1125 Colonel By Drive.

i	=	initial
ox	=	oxidizer
ref	=	reference conditions
s	=	fuel surface
t	=	turbulent quantity
theor	=	theoretical value
tot	=	total quantity
w	=	wall

Introduction

HYBRID rocket propulsion systems offer monetary, safety, and ease of storage advantages over their more traditional solid and bipropellant counterparts due to the use of an inert fuel grain that is kept separate from the oxidizer until motor ignition. Additionally, they typically have a higher specific impulse than solid rocket motors and can be restarted and throttled. At large scales, hybrid rockets are an unproven technology and have not been employed in commercial space launch applications. They have been used in target missiles and low-cost tactical missiles.

Hydrogen peroxide (HP) is a storable and nontoxic oxidizer that has been used in torpedoes and turbopumps as a gas generator, also in rocket engines for aircraft boost, and launchers (e.g., British Black Knight) [1]. Concentrated hydrogen peroxide has been experimentally investigated within the context of a hybrid rocket by various researchers. Wernimont and Heister [2] and Wernimont and Meyer [3] used polyethylene and 85%HP and 88%HP, respectively. Additionally, the latter presented data from previous work with HP, specifically one set of data pertaining to carboxyl terminated polybutadiene. Humble et al. [4] presented research performed to characterize the performance of polyethylene and 85%HP. Lund et al. [5] developed a gas generator fuel for a hybrid rocket to use HP as the oxidizer. Osmon [6] characterized the performance characteristics of 90%HP with lithium aluminum hydride. The outcome of these works is discussed in detail in later sections, as it pertains to the work presented herein.

The objectives of this work were twofold. The first objective was to produce data to characterize the performance of metallized hydroxyl terminated polybutadiene (HTPB)/unstabilized 90%HP in a hybrid motor configuration. To the authors' knowledge, no published data on the performance characteristics of metallized HTPB fuel with HP oxidizer exists in the open literature. The second objective was to develop a numerical model for a HTPB/90%HP hybrid motor to predict the regression rate of that propellant combination at various operating points and compare the results directly to experimental data. There has not been a publication in open literature of a numerical model to predict the regression rate of an HTPB fuel and HP propellant combination.

Experimental Program/Apparatus

The metallized fuel grains were 60%Al/40%HTPB and 60%Al-Mg/40%HTPB, by weight. The aluminum particle size was approximately 3 μm, whereas that of the 50%Al/50%Mg by weight alloy was approximately 120 μm. All fuel metal loading was at 60% by weight as this delivered the maximum theoretical performance with unstabilized 90%HP. The HTPB formulation used in these tests was Poly Bd R45HT. The fuel was mixed under a vacuum and cured for at least two weeks before use.

A test matrix was devised to characterize the performance of the various fuels with 90% HP. The tests were carried out at various chamber pressures, oxidizer to fuel ratios, and oxidizer mass fluxes. Two tests with nonmetallized HTPB fuel were performed to provide baseline measurements.

Catalyst Pack

The catalyst pack was composed of silver-plated nickel wire mesh screens that were treated with samarium nitrate to improve durability and efficiency. The screens were plated with a high current to achieve a rough surface finish to increase surface area and flow turbulence with the aim of improving the HP decomposition efficiency. The screens were arranged so as to optimize the oxidizer distribution and flow, from coarse to fine mesh starting at the sintered stainless steel injector plate. The screens were contained in a 316 L stainless steel assembly with an aluminum bulkhead separated by a linen phenolic heat shield and supported downstream of the injector by a wagon wheel type stainless steel support.

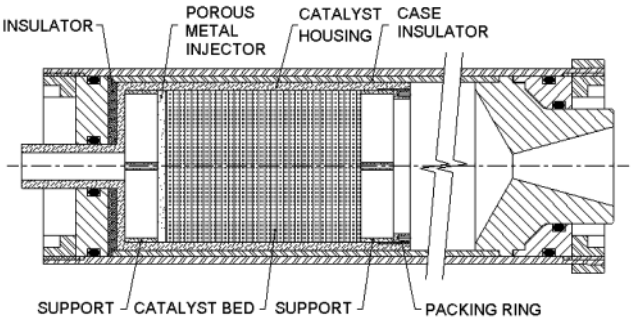

Fig. 1 Motor hardware schematic.

Rocket Motor

Figure 1 is a schematic of the motor hardware used for these tests. The motor was 75 mm in diameter and was a cartridge loaded reloadable system with modular forward and aft closures. The port diameter of the fuel grains was varied from 25.4–38.1 mm, and the length was 391.5 mm. The conical nozzles were compression molded using a silica phenolic resin, and a graphite insert was then bonded into the throat. The throat and nozzle diameters were then machined to the desired dimensions to achieve the required chamber pressure and to expand to atmospheric pressure. The motor casing was aluminum and lined with a paper phenolic insulator. The catalyst pack was inserted into this insulator and held in place with the forward closure. The precombustion chamber and reaction chamber components were linen phenolic tubing.

Thrust Bench Hardware and Instrumentation

Figure 2 shows a schematic of the test stand assembly. The main and preheat tanks were made of aluminum. All other thrust bench hardware was composed of Swagelok stainless steel 316 L tube, fittings, and valve components. The hardware was passivated per the manufacturer's instructions. The dump valve was used for emergency HP purge to a small tank in the test cell. Neither this nor the emergency water purge was required during any of the tests.

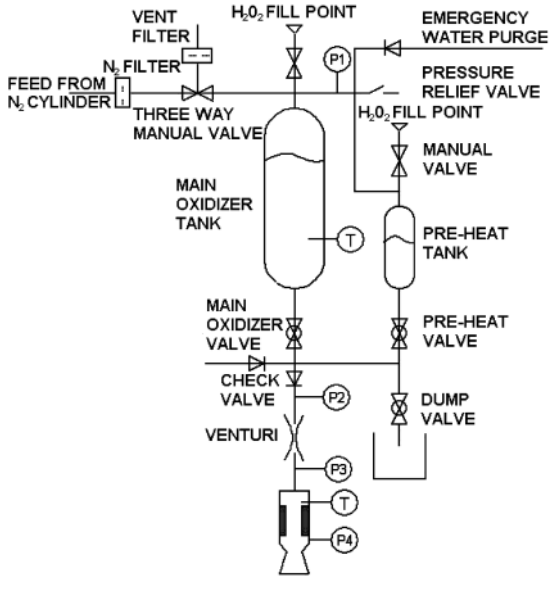

Fig. 2 Test stand assembly schematic.

The main oxidizer valve, preheat valve, and dump valve were all actuated pneumatically from the concrete enclosed control room in the test cell. A 5000 psia nitrogen cylinder with a regulator was used to pressurize the preheat and main oxidizer tanks using a three-way valve. When the system was not pressurized, it was automatically venting through this valve. The pressure relief valve was installed to allow venting of the system should the main or preheat tanks become contaminated, causing uncontrolled decomposition of the hydrogen peroxide during the time period between the tank fill and the start of the test. The pressure transducer upstream of the main oxidizer tank also provided a means by which to monitor the tank pressure for decomposition. Such an event did not occur during any of the tests.

The main oxidizer and preheat tanks were filled manually immediately before the start of each test, and both the manual fill valves and the vent filter valve were left open until the tank fill was complete. At that time the two fill valves were closed, and the vent valve was moved to the nitrogen fill position. During each test, a small amount of HP from the preheat tank was flushed through the catalyst pack to heat it before opening the main oxidizer valve and firing the motor.

A cavitating venturi was used to decouple any oscillations in chamber pressure from the mass flow rate of the oxidizer and ensured that it remained constant throughout the duration of each test. Once the test assembly was used with HP it was not flushed with water between tests to avoid the risk of contamination of the internal component surfaces.

The amplifier for the four pressure transducers sat outside the test cell, and shielded cables were used to deliver the signal to the control room. Each transducer had a slightly better than 2 mV/psi sensitivity. The thrust was measured using an Omega instruments load cell, and the signal was amplified and delivered to the control room underground. Data collection was accomplished using in-house DataCAD data acquisition software and a PCI data acquisition card. The card had 16 16-bit channels, each sampled at 1000 samples/s, and did not filter the sampled data before writing to disk. Five channels were used for each test: four for the pressure transducers and one for the load cell. The software allowed user programmable channel calibration coefficients enabling real-time pressure and thrust measurements to be displayed on screen before the initiation of data collection.

Data Analysis

Time averaged data reduction was performed by calculating parameter averages over the action time of the motor, consistent with the analysis presented in [2]. The motor start time was taken as the first movement on the chamber pressure trace that was greater than the rms fluctuation amplitudes, and the stop time was determined using the "tan-bisector" method as described in [1] and consistent with the method used in [2]. Integrals were calculated numerically using trapezoidal integration.

The temporally averaged oxidizer mass flux, total mass flux, oxidizer to fuel ratio, and chamber pressure were calculated as follows:

$$\overline{G_{\text{ox}}} = \frac{\Delta M_{\text{ox}}}{\overline{A_{\text{port}}} \cdot t_a} \tag{1}$$

$$\overline{G_{\text{tot}}} = \overline{G_{\text{ox}}} + \frac{\Delta M_f}{\overline{A_{\text{port}}} \cdot t_a} \tag{2}$$

$$\overline{OF} = \frac{\Delta M_{\text{ox}}}{\Delta M_f} \tag{3}$$

$$\overline{P_c} = \frac{1}{t_a} \int_{t_i}^{t_f} P_c \, \mathrm{d}t \tag{4}$$

Note that A_{port} was calculated by averaging the pre- and posttest fuel grain diameters.

The temporally averaged specific impulse was determined as follows:

$$\overline{I_{\text{sp}}} = \frac{\int_{t_i}^{t_f} F \, \mathrm{d}t}{g(\Delta M_{\text{ox}} + \Delta M_f + \Delta M_{\text{inert}})} \tag{5}$$

The expended inert mass of the precombustion and reaction chamber components was determined by weighing those components before and after each test.

Nozzle erosion was significant in the tests using the Al/HTPB fuel combination, likely due to the high-combustion temperature of the fuel as well as the significant amount of particulate matter observed in the nozzle exhaust. High-nozzle erosion with highly aluminized fuels was also noted by Lips [7]. Work by Bunker and Prince [8] indicated that a higher rate of nozzle erosion could be expected from hybrid motors than from solid motors, due to the higher concentration of oxygen containing species in the exhaust.

The $\overline{\eta c^*}$ calculated using conventional methods was erroneously high for tests with large amounts of throat erosion, even after correcting the data for erosion of the nozzle throat. Thus combustion efficiencies were estimated using thrust measurements as in Eq. (6) for all tests, allowing comparisons to be made between the fuel combinations. The parameter $Cf_{\text{theor}} = Cf_{\text{theor}}$ (nozzle area ratio, γ) and was taken as the average of the values obtained for the pre- and posttest conditions. The ratio of specific heats was calculated from equilibrium theory and varied insignificantly across the nozzle. Precedence for the necessity of the use of this technique is found in [7]. As the nozzle efficiency was assumed to be 1.0 in the calculation of Cf_{theor}, it is pertinent to note that the combustion efficiency obtained using this method included both losses due to inefficient combustion and thrust conversion efficiency or nozzle losses. The theoretical c^* and I_{sp} were calculated by assuming equilibrium chemistry and frozen flow conditions downstream of the nozzle throat.

$$\overline{\eta c^*} = \frac{1}{c^*_{\text{theor}} Cf_{\text{theor}}} \cdot \frac{\int_{t_i}^{t_f} F \, \mathrm{d}t}{\Delta M_{\text{ox}} + \Delta M_f + \Delta M_{\text{inert}}} \tag{6}$$

The temporally and spatially averaged fuel regression rate was determined based on fuel mass measurements taken before and after the test:

$$\bar{\dot{r}} = \frac{1}{t_a} \left\{ \left[\frac{\Delta M_f}{\pi \rho_f L_f} + \left(\frac{D_{\text{port},i}}{2} \right)^2 \right]^{\frac{1}{2}} - \frac{D_{\text{port},i}}{2} \right\} \tag{7}$$

The error analysis was performed using the method presented by Wernimont and Heister [9]. The experimental bias errors on performance parameters for a particular test are given in Table 1; these values are representative of those for the other tests in this study. The error for $\overline{\eta c^*}$ is not explicitly given as this parameter was calculated from thrust measurements. Table 1 also lists the most influential parameters affecting the derived error on the particular performance parameter.

Experimental Results and Discussion

Table 2 gives a summary of the tests performed and the results. High rates of nozzle erosion were observed in the tests with metallized fuels, likely due to the impingement of particulate matter in the exhaust on the nozzle surface. Figure 3 shows the data from all

Table 1 Experimental errors for test 14

Parameter	Error	Most influential variables
$\overline{I_{\text{sp}}}$	6.6 s, 2.7% of nominal	C_d, A_{venturi}
$\bar{\dot{r}}$	0.015 mm/s, 2.3% of nominal	D_{port}, t_a
$\overline{G_{\text{tot}}}$	5.9 kg/m^2 · s, 3.3% of nominal	D_{port}, C_d, A_{venturi}

Table 2 Summary of hybrid tests

Test	t_a, s	D_{throat}, mm initial/final	$\overline{P_c}$, kPa	$\overline{G_{ox}}$, kg/m^2 · s	$\overline{O/F}$	$\dot{\bar{r}}$, mm/s	$\overline{\eta c^*}$	$\overline{I_{sp}}$, s
			Fuel: 60%Al/40%HTPB					
1	8.70	9.0/11.5	2733	155	3.2	0.66	0.72	172
2	9.81	9.0/11.4	2615	143	3.0	0.67	0.74	175
3	8.33	9.0/14.8	2605	153	2.9	0.71	0.77	183
4	8.48	9.0/13.8	2421	116	3.4	0.53	0.73	171
5	7.73	15.0/16.5	1377	159	2.9	0.71	0.82	179
6	6.69	10.1/12.4	2636	155	2.4	0.87	0.89	213
7	3.86	10.5/12.8	3998	320	3.7	1.10	0.88	215
8	3.73	10.5/14.2	3956	235	3.7	0.94	0.89	219
			Fuel: 60%Al-Mg/40%HTPB					
9	6.72	9.0/9.0	3065	110	2.7	0.70	0.79	187
10	7.24	9.1/9.9	3078	148	2.3	0.93	0.84	200
11	3.73	10.5/11.6	4159	221	3.3	1.12	0.82	198
12	3.92	10.5/11.0	4105	298	3.3	1.27	0.83	200
13	6.53	15.0/15.0	1295	154	2.5	0.87	0.84	183
			Fuel: HTPB					
14	8.08	8.0/8.8	3691	150	5.1	0.67	0.90	213
15	6.99	8.0/8.0	3537	93	7.4	0.37	0.79	187

transducers for one of the 60%Al-Mg/40%HTPB tests. The ignition delay of approximately 1 s occurred in nearly all of the tests. This phenomenon was primarily an indication of the residence time required to bring the fuel to autoignition temperature. A short time delay of approximately 10–15 s occurred between the end of the preheat and the start of the main burn during each test to allow the data acquisition system to be started. This may have allowed the catalyst pack to cool slightly; the pack would then require a short time to return to full decomposition efficiency. The gradual decrease in chamber pressure during the motor burn was caused by erosion of the nozzle throat and occurred to varying degrees during all tests. The thrust trace was approximately constant, and this was due to the compensating effects of increasing throat area and decreasing chamber pressure on thrust. The rise in chamber pressure and thrust beginning at approximately 10.2 s into the motor action time shown in Fig. 3 occurred during every test. This was due to high-pressure nitrogen purging the motor when the main oxidizer tank had emptied, flushing out a volume of hydrogen peroxide that had accumulated in the catalyst pack. The particular test shown in Fig. 3 also exhibited anomalous spikes in the data from the pressure transducers both upstream and downstream of the venturi and from the load cell at approximately 5.9 s and 8.6 s. A bubble of HP being pushed through the venturi may have caused the sudden increase in chamber pressure and thrust.

Qualitative Observations

60%Al/40%HTPB Fuel

Although the tests run at lower chamber pressures all exhibited solidified fuel/slag agglomeration on the reaction chamber and nozzle inlet face, this effect was greatly reduced during the higher pressure tests. A coating of fine aluminum oxide powder remained on the fuel grain surfaces from all tests after firing. The low-pressure tests all exhibited visible pieces of matter in the exhaust.

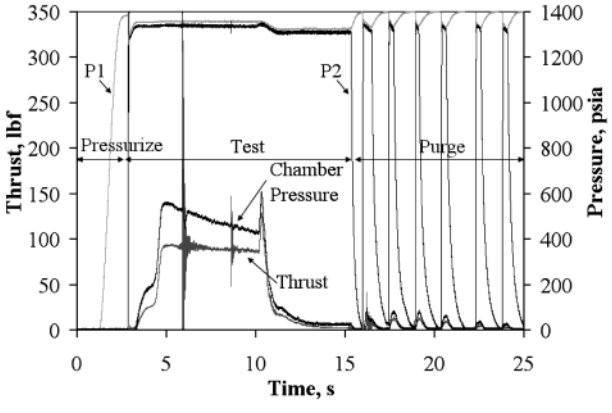

Fig. 3 Data from a 60%Al-Mg/40%HTPB test.

60%Al-Mg/40%HTPB Fuel

The low-pressure tests exhibited some solidified fuel/slag agglomeration on the reaction chamber and fuel grain; however, the effect was not as pronounced as with the 60%Al/40%HTPB fuel. The high-pressure tests showed a very clean grain burn surface and almost no agglomeration on any motor components.

HTPB Fuel

Both tests showed a clean grain surface after firing and no material agglomeration on any motor components.

Figure 4 shows a nozzle from a test with each fuel combination, along with a new nozzle for reference. The decrease of slag agglomeration with the Al-Mg fuel versus the Al fuel and the complete lack of any material agglomeration with the HTPB fuel is evident. Note that some of the agglomerated material on the nozzles was inadvertently removed during the disassembly of the motor.

Combustion Instability

Combustion instability was observed during the first five tests with Al/HTPB fuel, indicated by pressure oscillations with peak-to-peak amplitudes varying from 40 to 70 psia and frequencies of approximately 4 Hz. The average chamber pressures for these tests ranged from 200–400 psia. The instability was attributed to "chuffing": periodic shedding of accumulated molten Al_2O_3 from the grain surface and the ignition of virgin fuel [10]. It was

Fig. 4 Clockwise from top left: new, Al/HTPB test, Al-Mg/HTPB test, and HTPB test.

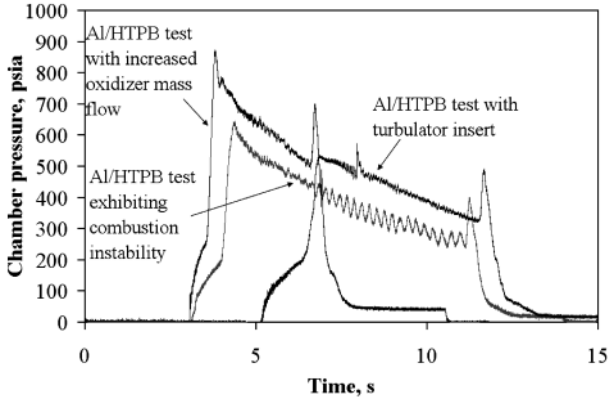

Fig. 5 Mitigation of Al/HTPB combustion instability.

hypothesized that a turbulator insert (or forward facing step), with a port diameter smaller than that of the grain port diameter, placed upstream of the grain entrance would induce recirculation and reduce the buildup of molten Al_2O_3 on the grain surface. A turbulator was added to one of the Al/HTPB tests, and the instability was mitigated. Additionally, it was noted that during the Al/HTPB tests at high-oxidizer mass flux (235 and 320 $kg/m^2 \cdot s$) no oscillations in chamber pressure were measured. The higher flow velocity relative to the grain and larger quantity of pyrolyzation gases liberated due to the increase in regression rate likely acted to prevent the formation of a molten Al_2O_3 layer on the grain surface during these tests. Figure 5 shows the chamber pressure oscillations for an Al/HTPB test and the subsequent reduction of these oscillations during the test with increased oxidizer mass flow, as well as during the test with the turbulator insert. The pressure traces are offset in time on this figure for clarity.

Chamber pressure fluctuations on the order of 2–5% of mean pressure were observed during all tests with both the Al-Mg/HTPB and HTPB fuels, indicating stable combustion.

Regression Rate

Figure 6 shows the measured regression rate for each fuel combination as a function of average total mass flux, $\overline{G_{\text{tot}}}$. Data from other relevant work is also shown for comparison purposes, and references are included in the figure legend.

An increase in regression rate was noted with the addition of the magnesium to the fuel composition; the regression rate was consistently approximately 0.2 mm/s greater at each oxidizer flux level tested than that of the 60%Al/40%HTPB fuel, possibly due to increased reactivity of the Al-Mg/HTPB fuel combination. The test with a turbulator upstream of the fuel grain demonstrated a regression rate increase of the 60%Al/40%HTPB fuel relative to the other tests, as the increased turbulence level resulted in an increase in convective

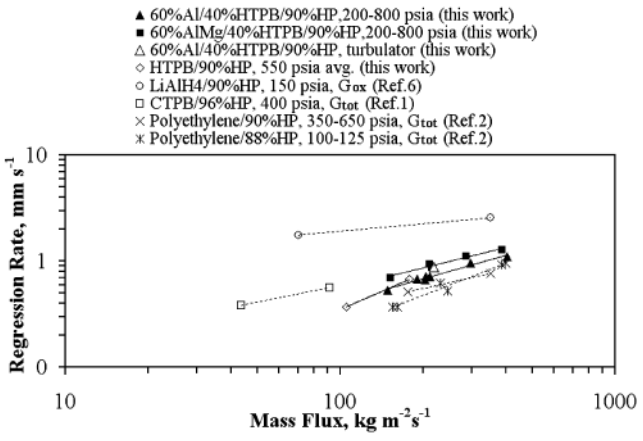

Fig. 6 Regression rate data for all tests and comparable data from the literature.

heat transfer to the fuel grain surface. This test is shown as a single data point on Fig. 6 and is not included in the correlation presented in Eq. (8) as the motor geometry for this test varied from that of the baseline configuration.

Although not included in Fig. 6, it is pertinent to note that work by Chiaverini et al. [11] showed that the addition of ultrafine aluminum powder (UFAL) to the fuel grain resulted in a regression rate increase of approximately 40% over baseline HTPB tests with gaseous oxygen. UFAL particle sizes are typically 0.05–0.1 μm.

Power law correlations for the regression rate data as a function of total mass flux for both the 60%Al/40%HTPB/90%HP and the 60% Al-Mg/40%HTPB/90%HP fuel combinations are given in Eqs. (8) and (9).

For the 60%Al/40%HTPB/90%HP combination,

$$\bar{\dot{r}} = 0.014\overline{G_{\text{tot}}}^{0.7} \text{ mm/s} \tag{8}$$

For the 60%Al-Mg/40%HTPB/90%HP combination,

$$\bar{\dot{r}} = 0.029\overline{G_{\text{tot}}}^{0.6} \text{ mm/s} \tag{9}$$

The exponent on total mass flux is less than the theoretical value of 0.8 predicted by turbulent heat transfer theory. This was likely due to a combination of radiative heat transfer from the highly metallized grains, as well as injector and motor geometry effects.

Combustion Efficiency

Table 3 gives a summary of the combustion efficiencies measured during the test program and presents results from other lab scale hybrid motor experiments for comparison purposes. The data for 95%$LiAlH_4$/5%polyethylene/90%HP from [6] and that for 60%Al/40%polyurethane/LOX from [7] showed combustion efficiencies comparable to those measured in this experiment. Two of the tests with Al/HTPB fuel were performed without reaction chambers, and those tests exhibited a low average $\overline{\eta c^*}$ value of 0.73. This was likely due to incomplete mixing of the reactants as a result of insufficient residence time of the propellant, and the values from those two tests were not included in Table 3. All subsequent tests used a reaction chamber, yielding L^* values of 1.6–4.3 m.

It was hypothesized that the low combustion efficiency of the 60% Al/40%HTPB fuel combination was a result of the formation of aluminum oxide (Al_2O_3) around the aluminum particles during the combustion process, inhibiting mass and heat diffusion to the interior of the particle. This effect has been recorded in literature repeatedly [6,7]. Because of the hypothesis that magnesium combusts in the gaseous phase [12], the combustion efficiency of the Al-Mg alloy fuel was expected to be higher than that of the aluminum fuel combination. However, the increased combustion time of the larger diameter particles relative to the chamber residence time [13] may have offset the gains of using magnesium in the fuel grain. Furthermore, the exhaust of the 60%Al-Mg/40%HTPB fuel combination contained two solid constituents: MgO and $MgAl_2O_4$. Failure of these oxides to condense completely in the combustion chamber would have resulted in a lower combustion temperature due to the loss of the latent heat of fusion from these reactions [14].

Table 3 Summary of combustion efficiencies of tested fuel/90%HP combinations and data from other relevant lab scale hybrid motor experiments

Fuel	$\overline{\eta c^*}$ range	$\overline{\eta c^*}$ average
60%Al/40%HTPB	0.73–0.89	0.83
60%Al-Mg/40%HTPB	0.79–0.87	0.83
HTPB	0.79, 0.90	0.85
Polyethylene/88%HP[a] [3]	0.87–0.98	0.93
95%$LiAlH_4$/5%polyethylene/90%HP [6]	0.79–0.86	0.83
60%Al/40%polyurethane/LOX[b] [7]	——	0.81

[a]Significant nozzle erosion occurred during these tests and may have affected the calculation of $\overline{\eta c^*}$.

[b]The motors used in this test used a mixing diaphragm in the post chamber to increase the combustion efficiency.

Lastly, because the estimation of c* efficiency used in this work included nozzle losses, the two phase exhaust of the metallized fuels likely played a large role in the reduction of the combustion efficiency for these tests.

The 60%Al/40%HTPB/90%HP propellant exhibited a possible dependence of combustion efficiency on pressure; the average efficiency measured for the two high-pressure tests ($\overline{P_c} = 580$ psia) was 0.89, 11.5% higher than the average efficiency measured for the lower pressure tests ($\overline{P_c} = 200$–400 psia) of 0.77. This effect could be attributed to the pressure dependence of aluminum particle burn time of $t_b \sim P^{-0.2}$ given in [13].

It should be noted that scaling effects have not been considered in this work, and previous work in this area has found that scaling effects are not negligible for laboratory scale motors nor for motors with a large particulate concentration in the exhaust products [6].

Overview of Numerical Model

The numerical model of the hybrid rocket motor (HRM) was constructed using a commercial computational fluid dynamics (CFD) package. Two models were built: one for each of the tests conducted with nonmetallized HTPB fuel. The main goals were to predict the regression rate and its spatial variation for the nonmetallized HTPB fuel at the initial operating conditions of the motor and to illustrate the interesting characteristics of the hybrid rocket motor flowfield: a turbulent boundary layer with blowing and combustion.

In the interest of expanding on the model described herein, the full three-dimensional Navier–Stokes equations were solved. However, for this first model, a 10 deg section of the domain was modeled and symmetry conditions were applied to produce an axisymmetric solution. The spent fuel grains examined during the experiments exhibited an axisymmetric character, supporting the validity of this approximation.

A steady-state solution was obtained for each model at the operating conditions present at the end of the ignition transient for the respective experimental test. Because the fuel surface is constantly regressing in a HRM, strictly speaking the motor is never operating at a steady state. However, the regression rate of the propellant combinations tested was several orders of magnitude lower than the mean velocity in the combustion chamber, and thus the steady-state approximation was valid for a specified set of operating conditions. Experimental verification of this point is given by Stamatov et al. [15].

To keep the solution process tractable, the geometry of the combustion chamber was simplified. The precombustion chamber and the subsequent forward facing step associated with the fuel grain, the reaction chamber, and the nozzle were not included; only the combustion chamber surrounded by the fuel grain was modeled. Similar geometrical simplifications were used in the numerical study by Venkateswaran and Merkle [16]. The implications of omitting of the precombustion chamber on the prediction of the average regression rate of the fuel are discussed further later in the paper.

Summary of Model Parameters

The model parameters are summarized in Table 4. A no-slip condition was specified at the fuel surfaces, and the surface temperature was given as temperature of the injected fuel. Symmetry boundary conditions were applied at the sides of the domain. The mass fractions of oxygen and water vapor at the inlet were based on those present in 90%HP, which was assumed to be fully decomposed upon exit from the catalyst pack. The temperature of the oxidizer at the inlet was set to the adiabatic decomposition temperature of 90% HP. The turbulence intensity at the inlet was taken from measurements reported by Strand and Ray [17] where it was found that the amplitude of the core flow turbulence at the inlet of the combustion chamber was approximately 10% of the mean velocity in cold flow simulation tests. This result was obviously strongly injector dependent, and the value was used in lieu of an experimental measurement. The reference pressure was set to the measured chamber pressure at the start of the test being modeled.

Table 4 Model parameters and boundary conditions

Model	HTPB14	HTPB15
Geometry		
Grain length	391.5 mm	391.5 mm
Port diameter	25.4 mm	38.1 mm
Reference pressure	4054 kPa	4040 kPa
Fuel density	907.1 kg/m^2	906.8 kg/m^3
Inlet		
Mass flow	0.00325 kg/s	0.00344 kg/s
Static temperature	1022 K	1022 K
Mass fraction: oxygen	0.423	0.423
Mass fraction: water	0.577	0.577
Turbulence intensity	0.1	0.1
Outlet		
Average static pressure	0 kPa	0 kPa
Fuel walls		
Emissivity	0.95	0.95
Diffuse fraction	1.0	1.0

Governing Equations

The governing equations were discretized using a finite volume method and iterated to a steady-state solution by marching the unsteady equations in pseudotime. The discretization was second-order accurate in space. The Favre averaged form of the Reynolds averaged Navier–Stokes equations used in the model was as follows [18].

Continuity:

$$\frac{\partial \bar{\rho}}{\partial t} + \frac{\partial(\bar{\rho}\,\tilde{u}_j)}{\partial x_j} = 0 \tag{10}$$

Species conservation:

$$\frac{\partial(\bar{\rho}\,\tilde{Y}_i)}{\partial t} + \frac{\partial(\bar{\rho}\,\tilde{u}_j\,\tilde{Y}_i)}{\partial x_j} = \frac{\partial}{\partial x_j}\left(\tilde{\Gamma}_i \frac{\partial \tilde{Y}_i}{\partial x_j}\right) - \frac{\partial}{\partial x_j}\left(\overline{\rho Y_i'' u_j''}\right) + S_i \tag{11}$$

Momentum conservation:

$$\frac{\partial(\bar{\rho}\,\tilde{u}_i)}{\partial t} + \frac{\partial(\bar{\rho}\,\tilde{u}_i\,\tilde{u}_j)}{\partial x_j} = -\frac{\partial \bar{\rho}}{\partial x_i} - \frac{\partial}{\partial x_j}\left(\overline{\tau_{ij}} + \overline{\rho u_i'' u_j''}\right) \tag{12}$$

Energy conservation:

$$\frac{\partial(\bar{\rho}\,\widetilde{h_{\text{tot}}})}{\partial t} + \frac{\partial(\bar{\rho}\,\widetilde{h_{\text{tot}}}\,\tilde{u}_j)}{\partial x_j} = \frac{\partial \bar{\rho}}{\partial t} - \frac{\partial}{\partial x_j}\left(\overline{q_j} - \sum_i^{N_C} \widetilde{\Gamma}_i\,\tilde{h}_i \frac{\partial \tilde{Y}_i}{\partial x_j} + \overline{\rho u_j'' h''}\right) - \frac{\partial}{\partial x_j}\left(\widetilde{u}_j\,\overline{\rho u_i'' u_j''}\right) \tag{13}$$

The molecular stress tensor and heat flux vector were defined as

$$\overline{\tau_{ij}} = -\bar{\mu}\left(\frac{\partial \tilde{u}_i}{\partial x_j} + \frac{\partial \tilde{u}_j}{\partial x_i}\right) \tag{14}$$

and

$$q_j = -\lambda \frac{\partial T}{\partial x_j} \tag{15}$$

The Reynolds stress tensor was given as

$$\overline{\rho u_i'' u_j''} = -\mu_t\left(\frac{\partial \tilde{u}_i}{\partial x_j} + \frac{\partial \tilde{u}_j}{\partial x_i}\right) \tag{16}$$

The turbulence species and energy fluxes were modeled as

$$\overline{\rho Y_i'' u_j''} = \frac{-\mu_t}{Sc_t}\frac{\partial \tilde{Y}_i}{\partial x_j} \tag{17}$$

and

$$\overline{\rho h'' u_j''} = \frac{-\mu_t}{Pr_t}\frac{\partial \tilde{h}}{\partial x_j} \tag{18}$$

It was assumed that the dilatation portion of the stress tensor was negligible as the Mach number in the combustion chamber was low. However, because of the nonisothermal character of the flowfield, the spatial variation of density as a function of temperature and composition was included. The contribution of the kinetic energy to the normal Reynolds stresses was neglected, as was the viscous diffusion and turbulent transport of kinetic energy in the energy equation. These assumptions are valid for flows with $\bar{\rho}k \ll \bar{P}$ or $k \ll \tilde{h}$, as in this study [19]. Lastly, the viscous stress work term was neglected relative to the Reynolds stress work term.

Computational Grid

A structured, predominantly hexahedral mesh was used for the model. The mesh was refined in the radial direction until the variation of the computed regression rate between subsequent meshes was shown to be less than the experimental error reported in Table 1. The mesh sizes for each model were $71 \times 811 \times 6$ and $96 \times 811 \times 6$ nodes, respectively. The first node away from the wall for each mesh was placed at 0.001 mm, corresponding to $y^+ < 1$.

Turbulence Model

The system of equations was closed using the shear stress transport (SST) turbulence model to quantify the eddy viscosity, μ_t. The SST model is a combination of the k–ω and k–ε models that has been shown to perform better than the k–ω and k–ε models alone [18]. The turbulent Prandtl, Schmidt, and Lewis numbers were defined as follows:

$$Pr_t = \frac{\mu_t Cp_t}{\lambda_t} = 0.9 \tag{19}$$

$$Sc_t = \frac{\mu_t}{\rho D_t} \tag{20}$$

$$Le_t = \frac{Sc_t}{Pr_t} = 1.0 \tag{21}$$

The transport equations for the kinetic energy, turbulence eddy frequency, and turbulence eddy dissipation were given as follows.

k–ε model:

$$\frac{\partial(\bar{\rho}k)}{\partial t} + \frac{\partial}{\partial x_j}(\bar{\rho}\,\tilde{u}_j\,k) = \frac{\partial}{\partial x_j}\left[\left(\mu + \frac{\mu_t}{\sigma_{k1}}\right)\frac{\partial k}{\partial x_j}\right] - \overline{\rho u_i'' u_j''}\frac{\partial \tilde{u}_i}{\partial x_j} - \frac{\mu_t}{\bar{\rho}^2}\frac{\partial \bar{\rho}}{\partial x_i}\frac{\partial \bar{\rho}}{\partial x_i} - \bar{\rho}\varepsilon \tag{22}$$

$$\frac{\partial(\bar{\rho}\varepsilon)}{\partial t} + \frac{\partial}{\partial x_j}(\bar{\rho}\,\tilde{u}_j\,\varepsilon) = \frac{\partial}{\partial x_j}\left[\left(\mu + \frac{\mu_t}{\sigma_\varepsilon}\right)\frac{\partial \varepsilon}{\partial x_j}\right] - C_{\varepsilon 1}\frac{\varepsilon}{k}\left(\overline{\rho u_i'' u_j''}\frac{\partial \tilde{u}_i}{\partial x_j} + \frac{\mu_t}{\bar{\rho}^2}\frac{\partial \bar{\rho}}{\partial x_i}\frac{\partial \bar{\rho}}{\partial x_i}\right) - C_{\varepsilon 2}\bar{\rho}\frac{\varepsilon^2}{k} \tag{23}$$

k–ω model:

$$\frac{\partial(\bar{\rho}k)}{\partial t} + \frac{\partial}{\partial x_j}(\bar{\rho}\,\tilde{u}_j\,k) = \frac{\partial}{\partial x_j}\left[\left(\mu + \frac{\mu_t}{\sigma_{k2}}\right)\frac{\partial k}{\partial x_j}\right] - \overline{\rho u_i'' u_j''}\frac{\partial \tilde{u}_i}{\partial x_j} - \frac{\mu_t}{\bar{\rho}^2}\frac{\partial \bar{\rho}}{\partial x_i}\frac{\partial \bar{\rho}}{\partial x_i} - \beta'\bar{\rho}k\omega \tag{24}$$

$$\frac{\partial(\bar{\rho}\omega)}{\partial t} + \frac{\partial}{\partial x_j}(\bar{\rho}\,\tilde{u}_j\,\omega) = \frac{\partial}{\partial x_j}\left[\left(\mu + \frac{\mu_t}{\sigma_\omega}\right)\frac{\partial \omega}{\partial x_j}\right] - \alpha\frac{\omega}{k}\left(\overline{\rho u_i'' u_j''}\frac{\partial \tilde{u}_i}{\partial x_j} + \frac{\mu_t}{\bar{\rho}^2}\frac{\partial \bar{\rho}}{\partial x_i}\frac{\partial \bar{\rho}}{\partial x_i}\right) - \beta\bar{\rho}\omega^2 \tag{25}$$

The eddy viscosity was then calculated using Eq. (26) or Eq. (27), depending on which model was used in a particular region. The regions applicable to each model were determined by means of blending functions, and the formulation of these functions is described in detail in [20].

$$\mu_t = C_\mu \bar{\rho}\frac{k^2}{\varepsilon} \tag{26}$$

$$\mu_t = \bar{\rho}\frac{k}{\omega} \tag{27}$$

The constants used in the SST model are summarized in Table 5.

Combustion Model

The products of fuel pyrolysis were taken to be entirely 1,3-butadiene (C_4H_6), as has been done by other researchers in [16,21,22]. Experimental data by Chiaverini et al. [23] gave the relative molar concentration of the pyrolysis products of HTPB at various surface temperatures. The data indicated that the composition was primarily 1,3-butadiene, and that the portion of 1,3-butadiene in the products decreased with increasing pyrolysis temperature. The material properties λ, μ, and Cp for the reactants and products were taken for a temperature range of $300 \le T \le 5000$ K from [24].

The combustion mechanism of 1,3-butadiene with hydrogen peroxide was approximated by a simplified two-step reaction model, given by Eq. (28) [22] and Eq. (29) [25].

$$C_4H_6 + 3O_2 \rightarrow 4CO + 2H_2O + H_2 \tag{28}$$

$$CO + 0.5O_2 \rightarrow CO_2 \tag{29}$$

The combined finite rate/eddy dissipation combustion model was used to model the rate of progress for each reaction step given in Eqs. (28) and (29). Both the eddy dissipation reaction rate and the finite rate reaction rate were computed at each node, and the lesser of the two for the particular nodal location was used. The eddy dissipation combustion model is based on the assumption of fast chemistry (a large Damköhler number), and it was used in this study under the assumption that the rate of combustion in turbulent diffusion flames is determined by the rate of mixing of the fuel and oxidizer on the molecular scale: the rate of dissipation of the eddies. The finite rate model is based on the assumption of complete mixing of the reactants at the molecular level.

The reaction rate given by the finite rate combustion model had the following form:

Table 5 Constants for the SST turbulence model

Constant	Value
$C_{\varepsilon 1}$	1.44
$C_{\varepsilon 2}$	1.92
C_μ	0.09
σ_{k1}	1.0
σ_{k2}	2.0
σ_ε	1.3
σ_ω	2.0
β	0.075
β'	0.09
α	5/9

$$F_{\mathrm{FR}} = A \cdot T^{B} e^{-\frac{Ea}{R_u T}} \tag{30}$$

The rate of progress for the reaction was then computed as

$$R_{\mathrm{FR}} = F_{\mathrm{FR}}[\mathrm{reactant}_1]^a[\mathrm{reactant}_2]^b \tag{31}$$

The pre-Arrhenius factor (A), temperature exponent (B), and activation energy (Ea) for the reaction were taken from [22]. The constants a and b were specified for each reaction step from [25]. These constants are summarized in Table 6 for the reaction given by Eq. (28). The reaction rate given in [25] for the CO oxidization reaction step had a functional dependency on H_2O and therefore could not be used in this study due to the abundance of water vapor in the oxidizer. The reaction rate for Eq. (29) was therefore determined solely via the eddy dissipation combustion model.

The rate of progress given by the eddy dissipation combustion model had the following form:

$$R_{\mathrm{EDC}} = A_{\mathrm{EDM}} \frac{\varepsilon}{k} \left(\min \frac{[\mathrm{reactant}]}{\nu'_{\mathrm{reactant}}} \right) \tag{32}$$

The constant $A_{\mathrm{EDM}} = 4$ after work presented in [26]. The values of k and ε were determined from the SST turbulence model. The results of the simulations showed that, in the system modeled herein, the rate of progress given by the eddy dissipation model was the limiting rate.

Fuel Ablation Model

To examine the variation of fuel surface temperature and regression rate along the length of the fuel grain, the fuel wall was divided into 10 evenly sized regions. A program was developed to compute the mass flow rate and temperature of the injected fluid individually at each region. The rate of ablation of the fuel surface was assumed to follow an Arrhenius-type law as given in Eq. (33); any heterogeneous surface reactions were neglected. The activation energy and preexponential factor for HTPB were taken from [23] and were valid for fuel surface temperatures greater than 722 K.

$$\dot{r} = A \cdot e^{-\frac{Ea}{R_u T_s}} \tag{33}$$

where $Ea = 4.91$ kcal/mol and $A = 11.04$ mm/s.

The energy balance at the fuel surface was given by Eq. (34). The wall heat flux in this equation was taken as the area weighted average value and output for each of the 10 regions of the fuel wall from the CFD solver. It included both the radiative and convective heat flux at the fuel wall. The energy of pyrolysis and specific heat capacity at constant pressure for HTPB were taken from [27]. The fuel density was determined experimentally. The conductive heat flux through the fuel grain was calculated assuming an exterior fuel grain temperature equal to the ambient temperature, which in this case was also equal to the fuel grain reference temperature. This approximation was valid for the initial conditions of the motor burn. It is also a good approximation for a quickly regressing fuel surface as the subsurface thermal boundary is thin in that case [28]. The form of the expression for the heat flux conducted through the fuel was obtained from [29].

$$q_w = \rho_f \dot{r}[h_d + Cp_f(T_s - T_{\mathrm{ref}})] + \rho_f \dot{r} Cp_f (T_s - T_{\mathrm{amb}}) \tag{34}$$

where $h_d = 430$ cal/g, $T_{\mathrm{ref}} = T_{\mathrm{amb}} = 298$ K, and $Cp_f = 0.39$ cal/gK.

The energy balance at the fuel surface, Eq. (34), was solved iteratively, and then the new value of T_s was passed back to the CFD solver upon restart. The iteration between the in-house code and the CFD solver was carried out until the change in temperature between subsequent solutions was less than 1.0 K. A temperature change of 1.0 K produced a change in regression rate of approximately 0.002 mm/s, which was an order of magnitude less than the experimental error on the regression rate shown in Table 1. The solution method was very similar to that presented by Serin and Gogus [21].

Table 6 Constants for finite rate chemistry model

Reaction	Constant	Value
Eq. (28)	A	8.8×10^{11} $\mathrm{cm}^{2.25}/\mathrm{s} \cdot \mathrm{mol}^{0.75}$
	B	0
	Ea/R_u	1.52×10^4 K
	a	0.15
	b	1.6

Radiation Model

The solution of the spectral radiative transfer equation was approximated using the P-1 radiative transfer model, also known as the differential approximation. The assumption of the model was that the radiation intensity was isotropic in space. The solid fuel was defined as a glossy opaque rubber due to the carbon black content, with an emissivity of 0.95 and a diffuse fraction of 1.0 [30]. The spectral dependency of the radiation intensity field was modeled using multiple gray gases. The model assumed that the functional dependence of the gas emissivity on temperature, partial pressure, and path length could be accurately correlated by assuming that the emissivity arose as a result of independent emission from four gray gases. The constituents accounted for in the model were C_4H_6, CO_2, CO, and H_2O.

The functional dependence of the emissivity for each gray gas was assumed to have the following form:

$$\epsilon_g = \sum_{j=1}^{N_g} a_{gj}(1 - e^{-K_j p_j L}) \tag{35}$$

This spectral model was also used in the numerical models presented by Serin and Gogus [21] and by Chiaverini et al. [30]. The coefficients for the model are summarized in Table 7, Eqs. (36) and (37).

$$a_{gj} = b_{1j} + 10^{-5} b_{2j} T_g \tag{36}$$

$$K_j = K_j(p_{\mathrm{H_2O}} + p_{\mathrm{CO_2}} + p_{\mathrm{CO}}) + K_{\mathrm{HC}j} p_{\mathrm{C_4H_6}} \tag{37}$$

Numerical Results and Discussion

The flame did not reach the centerline of the motor at the end of the fuel grain, indicating the need for mixing of the oxidizer rich core with the fuel remaining in the boundary layer upon exit of the grain. Figure 7 shows the variation of the flowfield density, temperature, and axial velocity in the near-wall region at 0.5 L for the HTPB14 model. The velocity overshoot characteristic of a turbulent combusting boundary layer is apparent in this figure. The velocity overshoot is the result of an interaction of the pressure gradient with the low-density flame region [31]. The flame is seen to be at approximately 2 mm from the wall at this axial motor location.

Contribution of Radiation to Wall Heat Flux

The portion of the wall heat flux due to convection is shown in Fig. 8 for both models. The increase in the radiative portion of the wall heat flux at the outlet of the model was due to the radiative boundary condition applied at the outlet, which specified the outlet as a blackbody radiating at the local fluid temperature. This condition was used in lieu of an experimental measurement of the radiative heat transfer from the components and flow downstream of the fuel grain.

Table 7 Coefficients for the gray gas spectral model

j	b_{1j}	b_{2j} [K^{-1}]	K_j [$\mathrm{m}^{-1} \cdot \mathrm{atm}^{-1}$]	$K_{\mathrm{HC}j}$ [$\mathrm{m}^{-1} \cdot \mathrm{atm}^{-1}$]
1	0.364	4.74	0	3.85
2	0.266	7.19	0.69	0
3	0.252	−7.41	7.4	0
4	0.118	−4.52	80	0

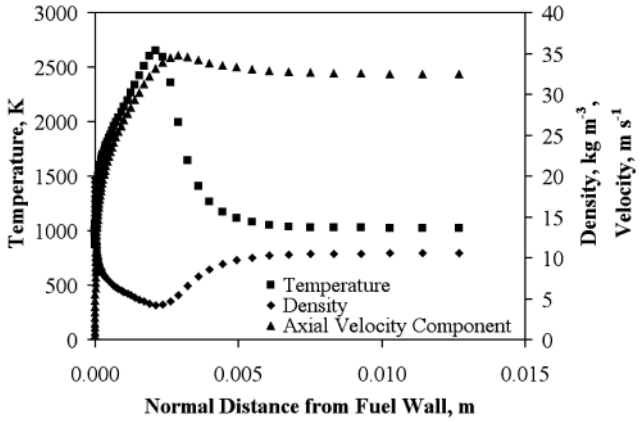

Fig. 7 HTPB14: Variation of flowfield properties normal to the fuel surface at 0.5 L.

It is clear that radiation plays a larger role in the total heat flux for the HTPB15 model, as it had a lower G_{ox}, and a larger D_{port}. The radiative heat flux contribution increased in the motor axial direction. Unique to the HP oxidizer/fuel combination, there is a high concentration of H_2O in the combustion chamber, and H_2O is one of the most important radiating gases in a hydrocarbon/oxygen system [30]. Thus, an increase in the portion of wall heat flux due to radiation can be expected for hybrid motors using a HP oxidizer relative to those using other oxidizers.

Comparison of Regression Rate to Experimental Results

Because of the elimination of the precombustion chamber from the model geometry, the vortex on the fuel surface driven by the flow of oxidizer over the fuel step was not included in the flowfield solution. The step was present in the experiment because the wall of the precombustion chamber was thinner than the web of the fuel grain. The oxidizer was expelled from the injector into the precombustion chamber and then flowed into the smaller diameter fuel grain. The regression rate increase due to this recirculation zone was not predicted in the current models. Figures 9 and 10 show the regression rate, surface temperature, and fuel mass injection profiles as a function of axial distance along the motor length. The experimentally measured spatially averaged regression rates and respective error bars are also shown as straight lines on this figure. The initial high regression rate predicted in both models was due to the high convective heat transfer to the fuel grain when the flame was very close to the fuel surface. The regression rate was seen to increase slightly with downstream distance, due to an increase in total wall heat flux with downstream distance. This effect has been measured experimentally and predicted numerically by researchers (see, for example, [16,32]).

Table 8 shows a summary of the regression rate calculated at each of the 10 regions along the fuel wall, for both the HTPB14 and HTPB15 models, corresponding to the points in Figs. 9 and 10. Also given are the spatially averaged regression rates for each model, the experimental regression rates for both tests, the experimental errors

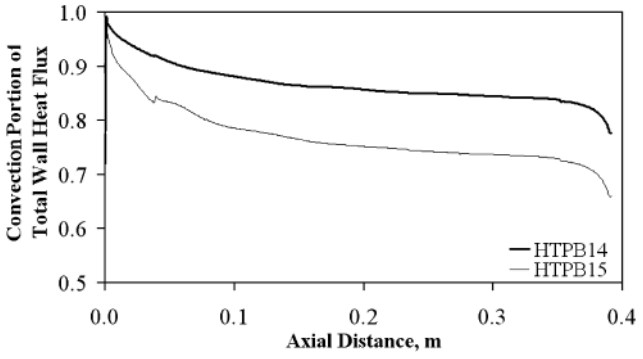

Fig. 8 Contribution of convection to total wall heat flux.

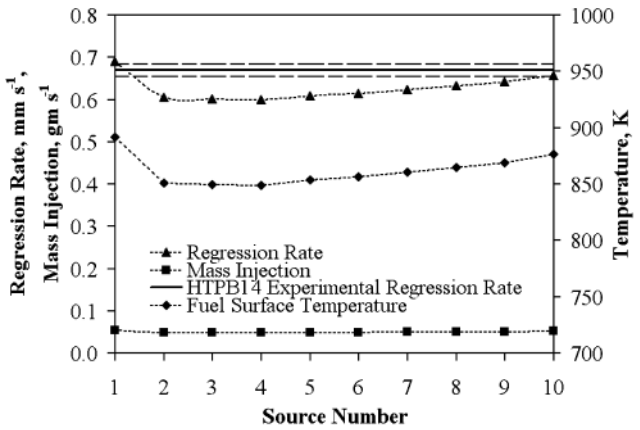

Fig. 9 HTPB14: Axial variation of fuel regression rate, surface temperature, and mass injection.

for both tests, and the percent difference between the calculated spatially averaged regression rate and the experimental regression rate.

The regression rate was overpredicted by HTPB15 and underpredicted by HTPB14. It is important to remember that these models were built using the motor operating conditions at the start of the tests, and the experimental data shown are the temporally and spatially averaged regression rate. As the burn progressed, the regression rate of the fuel would have decreased due to the decrease in total mass flux with the increase in port diameter. Therefore, in general, it is correct to say that the numerical results are an overestimation of the temporally averaged regression rate.

The overprediction of the experimental regression rate by the HTPB15 model is an indication that the model is a more accurate representation of the physics of the HRM than is the HTPB14 model. The increase in convective heat transfer due to the recirculation induced by the fuel step that was eliminated in the model geometry would have been low in the HTPB15 model, due to a smaller step height relative to the port diameter and a lower Reynolds number. The Reynolds numbers based on the chamber diameter upstream of the fuel grain were $Re_{HTPB14} = 436,600$ and $Re_{HTPB15} = 217,200$, respectively. The HTPB15 model, with $D_{port}/D_{prechamber} = 0.8$ produced a regression rate 10% higher than that measured experimentally, consistent with the initial conditions of the burn. However, when the step was an appreciable portion of the port diameter as in the HTPB14 model with $D_{port}/D_{prechamber} = 0.5$, the regression rate predicted by the model underpredicted the experimental data by 6%.

Conclusions

The 60%Al/40%HTPB fuel demonstrated an instability phenomenon called chuffing, caused by the accumulation of molten

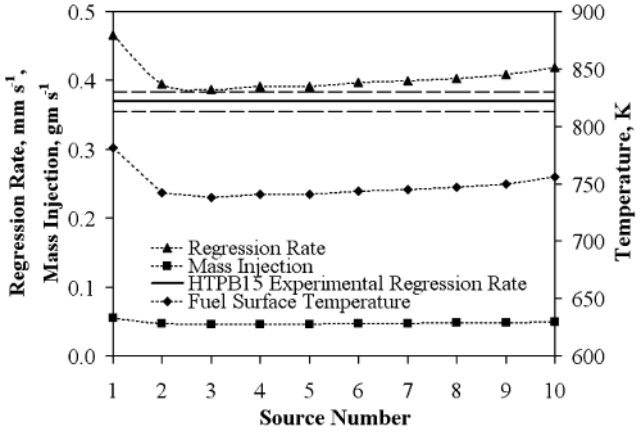

Fig. 10 HTPB15: Axial variation of fuel regression rate, surface temperature, and mass injection.

Table 8 Comparison of experimental and numerical results: regression rate

Model	HTPB14	HTPB15
Individual sources		
Source 1	0.689 mm/s	0.466 mm/s
Source 2	0.604 mm/s	0.395 mm/s
Source 3	0.601 mm/s	0.387 mm/s
Source 4	0.599 mm/s	0.392 mm/s
Source 5	0.609 mm/s	0.392 mm/s
Source 6	0.615 mm/s	0.397 mm/s
Source 7	0.624 mm/s	0.400 mm/s
Source 8	0.637 mm/s	0.403 mm/s
Source 9	0.641 mm/s	0.408 mm/s
Source 10	0.657 mm/s	0.419 mm/s
Numerical (av.)	0.627 mm/s	0.406 mm/s
Experimental	0.669 mm/s	0.369 mm/s
Difference	−0.042 mm/s	0.037 mm/s
Percent difference	−6.3%	10.0%
Experimental error	±0.015 mm/s	±0.014 mm/s

Al_2O_3 on the fuel grain surface. This effect was eliminated by adding a turbulator upstream of the fuel grain or by increasing the oxidizer mass flux. The addition of a turbulator also caused an increase in the regression rate of the 60%Al/40%HTPB fuel. A high rate of nozzle erosion was noted in the tests with 60%Al/40%HTPB fuel, consistent with the high temperature of combustion of that fuel and mechanical erosion of the nozzle throat by the large amount of particulate matter in the exhaust.

The average combustion efficiency, based on thrust efficiency, for the highly metallized fuel combinations was 0.83, consistent with other experimental data for highly metallized laboratory scale motors. The combustion efficiency was seen to increase with the increase of chamber pressure for the 60%Al/40%HTPB/90%HP propellant combination. A significant amount of slag agglomeration was noted on the motor components from the tests with 60%Al/40% HTPB/90%HP and to a lesser extent from the tests with 60%Al-Mg/ 40%HTPB/90%HP. This was an indication of insufficient mixing of the fuel and oxidizer streams or insufficient combustion chamber pressure owing to the pressure dependent burn time of the aluminum particles. The former could be rectified with the use of a mixing diaphragm downstream of the fuel grain.

The correlation of regression rate with total mass flux for the two metallized propellant combinations yielded mass flux exponents of 0.6 for 60%Al-Mg/40%HTPB/90%HP and 0.7 for 60%Al/40% HTPB/90%HP. These exponents indicated a deviation from turbulent convective heat transfer dominated behavior, likely due to the pressure dependence of the radiative portion of the wall heat transfer, motor geometry effects, and injector effects. The regression rate of the 60%Al-Mg/40%HTPB/90%HP combination was consistently approximately 0.2 mm/s higher than that of the 60% Al/40%HTPB/90%HP combination.

The numerical model predicted an increase of the regression rate with axial distance along the fuel grain for both HTPB/90%HP motors tested. The radiative heat transfer was shown to contribute significantly to the total wall heat transfer. The relative contribution of radiative heat transfer was shown to scale with port size and mass flux. The neglect of the fuel step at the fuel grain inlet was a good approximation for the motor with a small fuel web thickness relative to the fuel port diameter, $D_{\text{port}}/D_{\text{prechamber}} = 0.8$. The numerical results obtained herein indicate that computational fluid dynamics can be used to provide useful information about the spatial variation of the regression rate in a hybrid rocket motor with a homogeneous hydrocarbon fuel.

Acknowledgments

The authors would like to thank the Centre for Research in Earth and Space Technology (CRESTech) for supporting the study under Contract No. SP03TIP08. Additionally, the authors would like to thank Cesaroni Technology, Inc., and the Department of National Defense, Canada, for enabling this study to be completed under the title "HyperG-Hydro-reactive Gas Generator Hybrids."

References

[1] Sutton, G., and Biblarz, O., *Rocket Propulsion Elements*, 7th ed., Wiley, New York, 2001, Chaps. 2, 3, and 15.

[2] Wernimont, E. J., and Heister, S. D., "Combustion Experiments in Hydrogen Peroxide/Polyethylene Hybrid Rocket with Catalytic Ignition," *Journal of Propulsion and Power*, Vol. 16, No. 2, 2000, pp. 318–326.

[3] Wernimont, E. J., and Meyer, S. E., "Hydrogen Peroxide Hybrid Rocket Engine Performance Investigation," AIAA Paper 94-3147, June 1994.

[4] Humble, R. W., Bettner, M. P., and Sandfry, R. A., "Hystar Hybrid Rocket Program at the United States Air Force Academy," AIAA Paper 1997-2797, July 1997.

[5] Lund, G. K., Starrett, D. W., and Jensen, K. C., "Development and Lab Scale Testing of a Gas Generator Hybrid Fuel in Support of the Hydrogen Peroxide Hybrid Upper Stage Program," AIAA Paper 2001-3244, July 2001.

[6] Osmon, R. V., "An Experimental Investigation of a Lithium Aluminum Hydride—Hydrogen Peroxide Hybrid Rocket," *Chemical Engineering Progress Symposium Series*, Vol. 62, No. 61, 1966, pp. 92–102.

[7] Lips, H. R., "Experimental Investigation on Hybrid Rocket Engines Using Highly Aluminized Fuels," *Journal of Spacecraft and Rockets*, Vol. 12, No. 9, Sept. 1997, pp. 539–545.

[8] Bunker, R., and Prince, A., "Hybrid Rocket Motor Nozzle Material Predictions and Results," *Proceedings of the AIAA/SAE/ASME/ASEE 28th Joint Propulsion Conference and Exhibit*, AIAA Paper 1992-3591, July 1992.

[9] Wernimont, E. J., and Heister, S. D., "Reconstruction Technique for Reducing Hybrid-Rocket Combustion Test Data," *Journal of Propulsion and Power*, Vol. 15, No. 1, 1999, pp. 128–136.

[10] Greiner, B., and Frederick, R. A., Jr., "Hybrid Rocket Instability," AIAA Paper 1993-2553, 1993.

[11] Chiaverini, M. J., Serin, N., Johnson, D. K., Yeu-Cheng Lu, Kuo, K. K., and Risha, G. A., "Regression Rate Behavior of Hybrid Rocket Solid Fuels," *Journal of Propulsion and Power*, Vol. 16, No. 1, 2000, pp. 125–132.

[12] Gordon, D. A., in *Solid Propellant Rocket Research*, edited by M. Summerfield, Academic Press, New York, 1960, p. 271.

[13] Widener, J. F., and Beckstead, J. F., "Aluminum Combustion Modeling in Solid Propellant Combustion Products," AIAA Paper 1998-3824, 1998.

[14] Lips, H. R., "Metal Combustion in High Performance Hybrid Rocket Propulsion Systems," AIAA Paper 1976-640, July 1976.

[15] Stamatov, V., Honnery, D. R., and Soria, J., "Visualization of Flow Development in Hybrid Rocket Motors with High Regression Rates," *Journal of Propulsion and Power*, Vol. 21, No. 4, July–Aug. 2005, pp. 613–618.

[16] Venkateswaran, S., and Merkle, C. L., "Size Scale-up in Hybrid Rocket Motors," AIAA Paper 1996-0647, 1996.

[17] Strand, L. D., and Ray, R. L., "Hybrid Rocket Combustion Study," AIAA Paper 1993-2412, 1993.

[18] CFX-TASCflow, Primer Documentation, Ver. 2.10, AEA Technology, Waterloo, ON, Canada, 2000, pp. 87–113.

[19] Wilcox, D. C., *Turbulence Modeling for CFD*, DCW Industries, La Cañada, California, 1998, pp. 238–239.

[20] CFX-TASCflow, Theory Documentation, Ver. 2.10, AEA Technology, Waterloo, ON, Canada, 2000, pp. 38–41.

[21] Serin, N., and Gogus, Y., "Navier-Stokes Investigation on Reacting Flow Field of HTPB/O_2 Hybrid Motor and Regression Rate Evaluation," AIAA Paper 2003-4462, 2003.

[22] Cheng, G. C., Farmer, R. C., Hones, H. S., and McFarlane, J. S., "Numerical Simulation of the Internal Ballistics of a Hybrid Rocket Motor," AIAA Paper 1994-0554, 1994.

[23] Chiaverini, M. J., Harting, G. C., Yeu-Cheng Lu, Kuo, K. K., Peretz, A., Jones, S. H., Wygle, B. S., and Arves, J. P., "Pyrolysis Behavior of Hybrid-Rocket Solid Fuels Under Rapid Heating Conditions," *Journal of Propulsion and Power*, Vol. 15, No. 7, Nov.–Dec. 1999, pp. 888–895.

[24] McBride, B. J., Gordon, S., and Reno, M. A., "Coefficients for Calculating Thermodynamic and Transport Properties of Individual Species," NASA TM-4513, Oct. 1993.

[25] Westbrook, C. K., and Dryer, F. L., "Simplified Reaction Mechanisms for the Oxidization of Hydrocarbon Fuels in Flames," *Combustion Science and Technology*, Vol. 27, Nos. 1–2, 1981, pp. 31–43.

[26] Magnussen, B. F., and Hjertager, B. H., "On Mathematical Modeling of

Turbulent Combustion with Special Emphasis on Soot Formation and Combustion," *Sixteenth International Symposium on Combustion*, The Combustion Institute, Pittsburgh, PA, Aug. 1976, pp. 719–728.

[27] Lengelle, G., Fourest, B., Godon, J. C., and Guin, C., "Condensed Phase Behavior and Ablation Rate of Fuels for Hybrid Rocket Propulsion," AIAA Paper 1993-2413, 1993.

[28] Chiaverini, M. J., Serin, N., Johnson, D. K., Yeu-cheng Lu, Kuo, K. K., and Risha, G. A., "Thermal Pyrolysis and Combustion of HTPB-Based Solid Fuels for Hybrid Rocket Motor Applications," AIAA Paper 1996-2845, 1996.

[29] Kubota, N., "Survey of Rocket Propellants and Their Combustion," *Fundamentals of Solid-Propellant Combustion*, edited by K. K. Kuo and M. Summerfield, Vol. 90, Progress in Aeronautics and Astronautics, AIAA, New York, 1984, pp. 38–40.

[30] Chiaverini, M. J., Kuo, K. K., Peretz, A., and Harting, G. C., "Regression-Rte and Heat-Tansfer Correlations for Hybrid Rocket Propulsion," *Journal of Propulsion and Power*, Vol. 17, No. 1, 2001, pp. 99–110.

[31] Yam, C., and Dwyer, H., "Investigation of the Influence of Blowing and Combustion on Turbulent Wall Boundary Layers," *AIAA Journal*, Vol. 27, No. 3, March 1989, pp. 370–372.

[32] Dean, D. L., "Effects of Fuel Formulation on Regression Performance in Hybrid Motors," AIAA Paper 19-0886, Jan. 1996.

S. Son
Associate Editor